Short-Range Correlations in Magnetite above the Verwey Temperature

Alexey Bosak,[1] Dmitry Chernyshov,[2] Moritz Hoesch,[3] Przemysław Piekarz,[4] Mathieu Le Tacon,[5] Michael Krisch,[1] Andrzej Kozłowski,[6] Andrzej M. Oleś,[5,7] and Krzysztof Parlinski[4]

[1]*European Synchrotron Radiation Facility, 6 rue Jules Horowitz, F-38043 Grenoble Cedex, France*
[2]*Swiss-Norwegian Beam Lines at ESRF, 6 rue Jules Horowitz, F-38043 Grenoble Cedex, France*
[3]*Diamond Light Source, Harwell Campus, Didcot OX11 0DE, Oxfordshire, England*
[4]*Institute of Nuclear Physics, Polish Academy of Sciences, Radzikowskiego 152, PL-31342 Kraków, Poland*
[5]*Max-Planck-Institut für Festkörperforschung, Heisenbergstrasse 1, D-70569 Stuttgart, Germany*
[6]*Faculty of Physics and Applied Computer Science, AGH-University of Science and Technology, Aleja Mickiewicza 30, PL-30059 Kraków, Poland*
[7]*Marian Smoluchowski Institute of Physics, Jagellonian University, Reymonta 4, PL-30059 Kraków, Poland*

(Received 20 November 2013; revised manuscript received 16 January 2014; published 17 March 2014)

Magnetite, Fe_3O_4, is the first magnetic material discovered and utilized by mankind in Ancient Greece, yet it still attracts attention due to its puzzling properties. This is largely due to the quest for a full and coherent understanding of the Verwey transition that occurs at $T_V = 124$ K and is associated with a drop of electric conductivity and a complex structural phase transition. A recent detailed analysis of the structure, based on single crystal diffraction, suggests that the electron localization pattern contains linear three-Fe-site units, the so-called trimerons. Here, we show that whatever the electron localization pattern is, it partially survives up to room temperature as short-range correlations in the high-temperature cubic phase, easily discernible by diffuse scattering. Additionally, *ab initio* electronic structure calculations reveal that characteristic features in these diffuse scattering patterns can be correlated with the Fermi surface topology.

DOI: 10.1103/PhysRevX.4.011040

Subject Areas: Condensed Matter Physics, Materials Science, Strongly Correlated Materials

I. INTRODUCTION

Discovered in the first half of the 20th century, the Verwey transition in magnetite [1] remains one of the most intriguing phenomena in solid-state physics. Magnetite is a ferrimagnetic spinel with anomalously high Curie temperature $T_C = 850$ K. Hence, it is viewed as an ideal candidate for room-temperature spintronic applications. It crystalizes in the inverse spinel cubic structure, with two types of Fe sites: the tetrahedral A sites and the octahedral B ones [2–8]. At $T_V = 124$ K, a first-order phase transition occurs as the electric conductivity drops by 2 orders of magnitude [1] with the simultaneous change of the crystal structure from the cubic to monoclinic symmetry [2] and with spectacular anomalies in practically all physical characteristics [3–8]. The low-temperature structure of magnetite, as deduced from recent studies, is identified to be of monoclinic Cc space group symmetry, with a complex displacement pattern [9].

In recent years, the main research effort was focused on the low-temperature phase in order to elucidate the character of charge ordering (CO) first proposed by Verwey as the primary mechanism of the phase transition. From these investigations, a complex picture of a low-symmetry state arises involving charge, orbital, and lattice degrees of freedom [6–21]. Diffraction studies performed below T_V have revealed a fractional charge disproportionation [6,7], with a CO and associated orbital ordering on B sites, which can be explained by strong Coulomb interactions [10,11] that amplify the coupling between $3d$ electrons and lattice deformation [12–14]. This charge and orbital order was recently suggested to exist in the form of so-called trimerons, distributed over three octahedral Fe sites, and coupled to the lattice distortion [9].

Above the Verwey transition, where the inverse spinel structure, with Fe^{3+} ions in A sites and B sites in a mixed-valence $Fe^{2.5+}$ state, is realized, several observations indicate the existence of short-range order of polaronic character [22–25]. This correlated state is reflected in the critical softening, on cooling, of the c_{44} elastic constant [26,27], softening of the surface phonons [28], critical diffuse scattering [29–34], and anomalous phonon broadening [35]. Furthermore, the quasielastic character of neutron scattering suggests low-energy fluctuations of the lattice distortions coupled to electrons [31,32].

This short-range order above the Verwey transition, its subtleties, and its connection to the low-temperature phase

is still not completely understood. Thus, to gain further insight into the transition, the observation of this short-range order and its coupling to the electronic properties of the t_{2g} minority-spin states of the Fe octahedral (B) atoms (which contribute to the metallic state above the Verwey transition) is crucial. We will show below that Fermi surface nesting features may be responsible for the observed short-range order.

Typical spotlike diffuse scattering is reported a few kelvin above T_V at positions $q = (h, 0, l + 1/2)$, which become Bragg reflections below the phase transition [29]. Another type of diffuse scattering with a disklike shape is revealed close to the Γ and X points over a wide range of temperatures [30–32]. In order to clarify the exact shape and behavior of diffuse scattering, as well as to unambiguously demonstrate its relation to the low-symmetry structure, we study the evolution of x-ray diffuse scattering in magnetite as a function of temperature down to the Verwey transition and below. With the use of a state-of-the-art large area detector (PILATUS 6M), a detailed three-dimensional (3D) reciprocal space mapping can be performed, revealing an extremely rich diffuse scattering pattern, inherited from the complex low-temperature structure below the Verwey transition.

The remainder of the paper is organized as follows. The experimental part is described in Sec. II. In Sec. III, we give the details of the performed *ab initio* electronic structure calculations that serve to determine the Fermi surface in the metallic state. In Sec. IV, we present and discuss the obtained results of diffuse scattering experiments (Sec. IV A) and present the consequences of charge ordering (Sec. IV B). The main results for the Fermi surface of magnetite are given in Sec. IV C. There, we also report a remarkable agreement between the experimentally obtained nesting signatures in the reciprocal space of magnetite and the calculated Fermi surface nesting. The paper is summarized in Sec. V.

II. EXPERIMENT

The single crystalline magnetite samples were grown at Purdue University by the skull melter, cruciibleless technique [36]. This allowed control of the oxygen partial pressure during growth, thereby ensuring that the melt remains within the stability range of the material. After preparation, the crystals were subjected to subsolidus annealing under CO/CO_2 gas mixtures to establish the appropriate metal/oxygen ratio [37]. Because of rapid quenching from high temperatures, this procedure generates octahedral defects and introduces stress [38]. However, the stoichiometry is maintained and most of the low-temperature electronic processes are not affected, as is evidenced by the sharp Verwey transition with high $T_V \sim 124$ K; see Fig. 1 in the Supplemental Material [39].

Similar low-temperature (low-T) processes were revealed by microscopic probes [40,41] for samples prepared in a different way. Thus, electronic processes that cause diffuse scattering result from the intrinsic properties of magnetite, and not from particular preparation conditions.

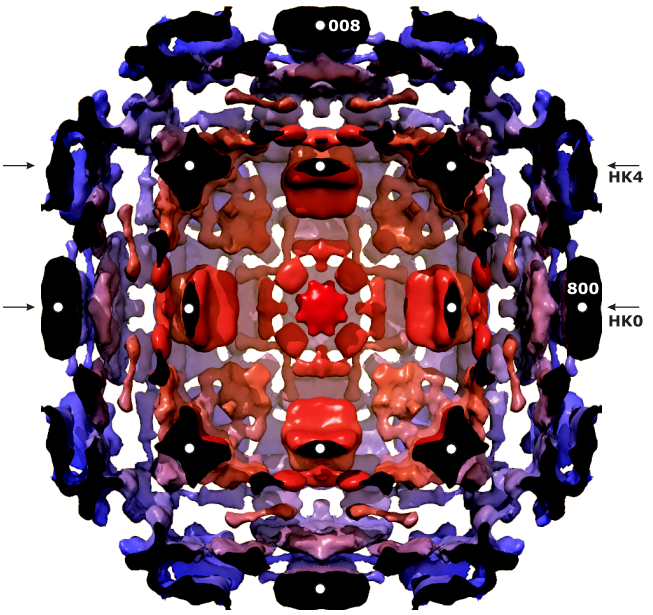

FIG. 1. Isosurface representation of diffuse scattering in magnetite slightly above T_V. Color represents the distance to the (000) node; diffuse clouds in the proximity of weak Bragg spots are removed. The half-space above the H0L plane is removed. $|Q|$-dependent intensity scaling is applied for the purpose of better visualization. White circles mark strong Bragg reflections in the H0L plane, and arrows denote HK0 and HK4 cuts perpendicular to the image plane.

Prior to the experiment, the nearly stoichiometric crystals (nominal $\delta = 0.00003$ and $\delta = -0.0001$ for $Fe_{3(1-\delta)}O_4$) were mechanically made into the shape of a needle and etched down to 50 μm diameter with HCl in order to remove the damaged surface layer. Both samples gave identical results; the data for $\delta = -0.0001$ are presented and referred to. It is noteworthy that the diffuse patterns are stable with respect to the nonstoichiometry above T_V, while below T_V the same pattern can coexist with the superstructure; see Fig. 2 in the Supplemental Material [39].

The scattering data were collected at room temperature, $T = T_V + 2.5$ K and $T = T_V - 2.5$ K, and a number of intermediate temperatures (155, 195, 245 K) in shutterless mode with the PILATUS 6M detector [42]. The preliminary measurements were performed at beam line X06SA at the SLS and the follow-up data recording took place at beam line ID29 at the ESRF; in both cases, a wavelength of 0.7 Å was employed. The crystal was mounted on a horizontal rotation stage, and the diffuse scattering patterns were recorded with an increment of 0.1° over an angular range of 360° with 0.25 s exposure per frame, i.e., 15 min per full data set.

The experimental geometry was refined with the help of the CrysAlis software [43] that was also used for the

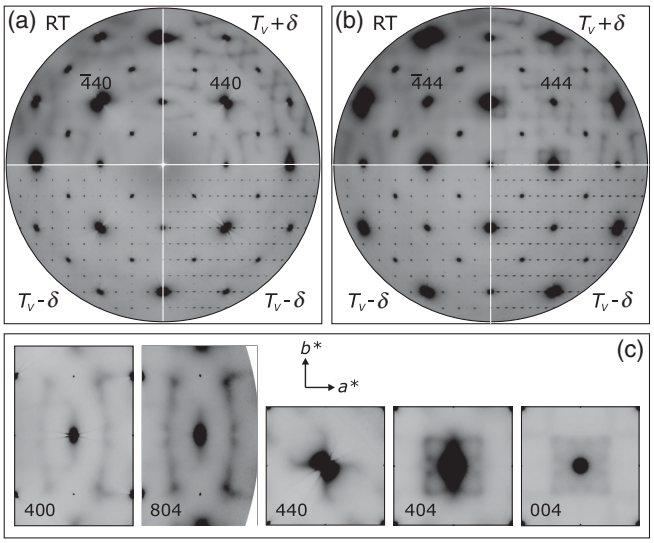

FIG. 2. Diffuse scattering in magnetite at variable temperature. Magnetite reciprocal space cuts HK0 (a) and HK4 (b) are shown at room temperature (RT), slightly above ($T_V + \delta$) and below ($T_V - \delta$) the Verwey transition, with $\delta \sim 2.5$ K. Left-hand bottom panels: Sections perpendicular to the cell doubling direction. Right-hand bottom panels: Sections parallel to the cell doubling direction. Selected regions of interest (see text) are shown in (c) together with the unit cell vectors $a*$ and $b*$. The room-temperature cut is scaled taking into account the thermal expansion for visualization purposes; the labels in (c) denote the central Bragg spot. Cubic $m3m$ (above T_V) and tetragonal $4/mmm$ (below T_V) Laue symmetries are applied.

preliminary data evaluation. The reconstruction of the selected reciprocal space layers was performed with a locally developed software. The reconstructed volume was averaged with its symmetrically equivalent orientations employing the Laue symmetry of the average structure, thus improving the signal-to-noise ratio and removing the gaps between individual detector elements. The low-temperature data were collected utilizing an attenuator in order to avoid intensity saturation effects of the superstructure reflections.

III. ELECTRONIC STRUCTURE CALCULATIONS

Ab initio calculations of the Fermi surface were performed in the cubic inverse-spinel unit cell within the generalized-gradient approximation of the density functional theory using the all-electron WIEN2K code [44]. The linearized augmented plane wave basis with local orbitals was expanded to $k_{\max}$ given by $rk_{\max} = 7$ outside the atomic spheres with radius $r = 1.63$ a.u. for oxygen and $r = 1.83$ a.u. for iron.

A symmetry-reduced grid of $21 \times 21 \times 21$ points in momentum space was used for convergence of the total energy. The lattice parameter was relaxed to 15.871 a.u., which agrees very well with the experimental value 15.862 a.u. A well-converged ferrimagnetic arrangement was obtained, with opposite orientations of magnetic moments in the A and B sites, as observed in magnetite below the Curie temperature $T_C = 850$ K.

IV. RESULTS AND DISCUSSION

A. Diffuse scattering experiments

Figure 1 shows the representative diffuse features of magnetite slightly above T_V in the form of isosurfaces. The strong main lattice Bragg spots are not visible here because their intensity is much higher than the value of the isosurfaces. The isolated diffuse clouds centered on weak Bragg reflections are removed, thus only keeping extended and/or interconnected fragments. Already, this overview shows that the diffuse scattering cannot be reduced to simple objects, such as spots and disks, but, in contrast, reveals a rich structure which is discussed in detail below.

The results of the diffuse scattering measurements in magnetite for two representative reciprocal space cuts of the HK0 plane (left-hand panel) and HK4 plane (right-hand panel) are presented in Fig. 2. In addition to the contributions from thermal diffuse scattering, which arises predominantly from acoustic phonons and is centered around Bragg reflections, we observe other distinct diffuse features already at room temperature. On cooling, these features gradually become stronger and sharper (see Fig. 2, upper panels).

Detailed mapping allows recovery of the actual shape of these features, previously reported as spotlike and disklike objects [30–32]. Among the most remarkable features, we can list squares centered on the strongest Bragg reflections of the spinel (400, 800, 440, and 448) structure and arcs (nearly symmetric pairs are visible around 400 and 804 reflections). Some distinct objects are shown in Fig. 2(c). It is worth noting that the local maxima of diffuse intensity never appear at X points, but are, rather, shifted aside, to incommensurate positions.

Below the Verwey temperature, the diffuse intensity collapses into the superstructure Bragg reflections. While the real symmetry of the low-temperature phase is monoclinic, the diffraction pattern appears similar to that of a tetragonal structure. The modulation vector corresponding to the doubling of the unit cell in the c direction appears in only one direction of the three $\langle 100 \rangle$-type equivalents; thus, not more than 8 out of 24 twins allowed by the symmetry are apparent. This is illustrated by the lower panels of Fig. 2, where the structure is considered to be pseudotetragonal with corresponding Laue symmetry operations applied.

B. Consequences of charge ordering

We now compare the measured diffuse intensities with the scattering pattern of the ordered phase below T_V (intensities taken from Ref. [9]). In the same linear gray scale, the superstructure reflections are highly saturated. Thus, for the graphical representation, we perform the following data transformations: (i) symmetrization by the

operations of the $m3m$ point group, (ii) attenuation of cubic spinel Bragg reflections to a constant level, and (iii) convolution of all the reflections with a Gaussian profile. In this way, the intensity of superstructure reflections is visualized via both the size and the intensity of spots; the result of this procedure is shown in Figs. 3(a) and 3(b) (lower panels) and compared to the diffuse data set taken slightly above T_V. A comparison of the 3D intensity distribution above and below the transition is shown in Figs. 3(c) and 3(d).

The qualitative similarity is apparent: all diffuse features have their counterparts with proportional intensity in the low-T diffraction at roughly the same Q, and vice versa. Subsets of strong reflections form the squares around the strongest spinel reflections, as does the diffuse scattering above T_V; the diffuse arcs, in turn, transform to the chains of spots. This means that the basic short-range ordering pattern is inherited from the low-T structure, while the transition is accompanied by the loss of commensurability (note that the X points are avoided).

The characteristic length estimated from the width of diffuse features varies from ~2 unit cells (u.c.) of the prototype cubic structure at $T_V + 2.5$ K to a value slightly

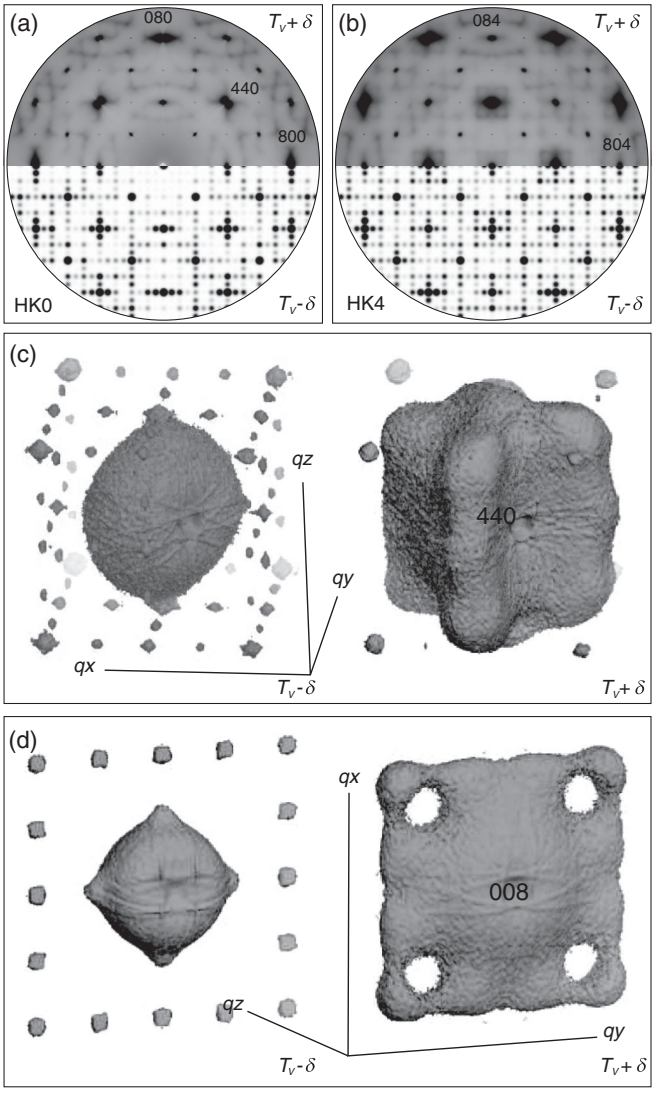

FIG. 3. Top: Similarity of scattered intensity distribution in magnetite above and below the Verwey transition. Magnetite reciprocal space cuts, (a) HK0 and (b) HK4, are compared for temperatures above T_V ($T_V + \delta$, upper part) and below T_V ($T_V - \delta$, lower part), with $\delta \sim 2.5$ K. Gaussian blurring is applied to the superstructure reflections; main reflections are replaced by constant intensity peaks to avoid masking the superstructure-related features. Middle and bottom panels: Isosurface representation of diffuse scattering in magnetite as given in the proximity of the (c) (440) and (d) (008) node. Indices and vector lengths are given in r.l.u. of the cubic structure. Cubic $m3m$ Laue symmetry is applied. Artificial twinning of the low-temperature data recovers the cubic symmetry.

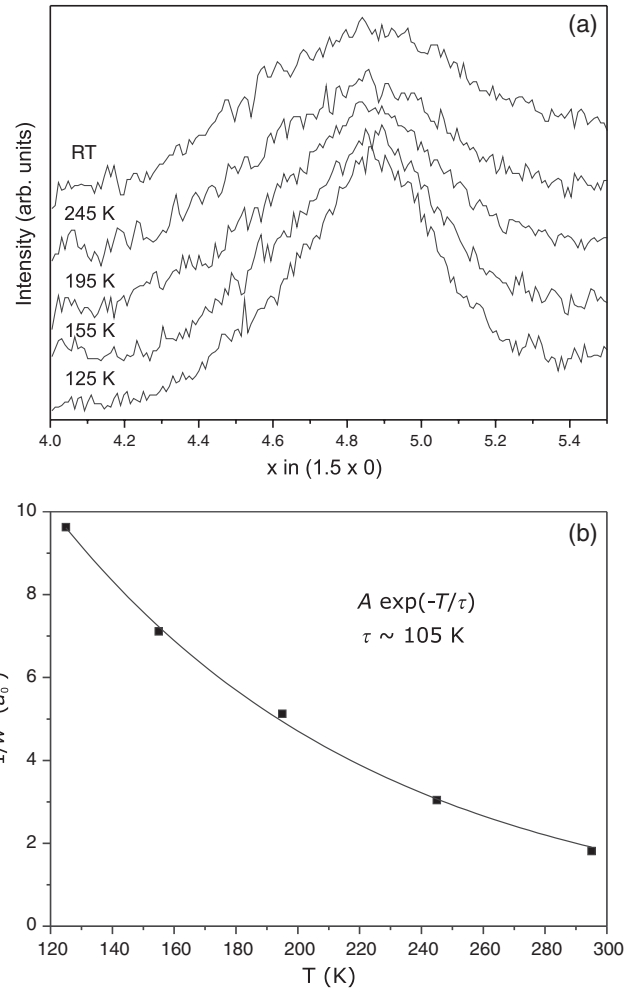

FIG. 4. Temperature dependence of characteristic diffuse intensity in magnetite: (a) linear scans across the arclike diffuse feature of magnetite for temperatures between T_V and a room temperature, and (b) the temperature decay of the derived $1/w^3$ value (symbols), together with its exponential fit $A\exp(-T/\tau)$ (solid line). Here, w is the width of the linear diffuse scattering scans and a_0 denotes the lattice parameter of the cubic lattice.

larger than ~1 u.c. at room temperature (see Fig. 4). Thus, the ordering pattern cannot be reduced to the trimeron features [9], but rather to complexes of trimerons. Therefore, our study supports the polaron picture, and we can state that its structure is in reality much more complex than ever expected previously.

C. Fermi surface

Cooling down to the Verwey temperature provokes condensation of these dynamic objects to the monoclinic structure with static charge ordering. The entropy change at T_V should be further reduced compared to the trimeron-based estimates [9]. The local symmetry of the complexes can be lower than cubic, but the average cubic symmetry is recovered by nanotwinning.

Such a complex CO, which cannot be reduced to a few frozen phonon modes, can, at least partially, be explained by the Fermi surface topology. In fact, it has been shown that the short-range order part of the diffuse scattering can reveal details about the electronic structure [45,46]. This is caused by an anomaly in the static susceptibility of the conduction electrons at scattering vectors, $k = 2k_F$ (k_F denotes the Fermi wave vector), and, therefore, in the Fourier transform of the pair-interaction potential. The effect can become particularly pronounced if different portions of the Fermi surface are connected by a single scattering vector (Fermi surface nesting).

In order to validate our hypothesis, a number of nesting constructions based on our *ab initio* calculations were evaluated for intraband and interband transitions. For the nesting construction, we use $|\nabla\chi_q|$, where

$$\chi_q = \sum_k \frac{n_F(\varepsilon_k) - n_F(\varepsilon_{k+q})}{\varepsilon_k - \varepsilon_{k+q}} \tag{1}$$

is the real part of the bare spin susceptibility (Lindhard function) [47] at frequency $\omega \to 0$; here,

$$n_F(\varepsilon) = \frac{1}{\exp(\frac{\varepsilon}{k_B T}) + 1} \tag{2}$$

stands for the Fermi-Dirac distribution function (k_B is the Boltzmann constant), and ε denotes the kinetic energy of the electrons (the chemical potential is set to zero). The total Fermi surface has a quite complex shape, traced in Fig. 5(a) as the isosurface of $\sum_n \exp(-\varepsilon_{k,n}^2/\alpha)$, where n refers to the band number, and α is chosen to smear out the discretization artifacts. We find that the scattering within the minority-spin t_{2g} band shown in Fig. 5(b) can account for the observed diffuse scattering pattern.

Figure 6 confronts the reciprocal space patterns of the HK0 and HK4 planes with the Fermi surface nesting construction. It can be appreciated that most of the non-thermal-diffuse features can be associated with efficient nesting vectors (dark gray in the right-hand panels). The

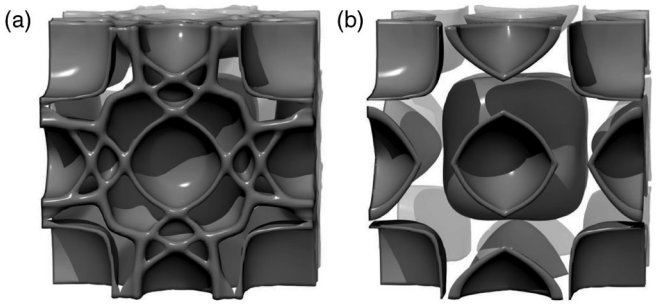

FIG. 5. Fermi surface of magnetite in the cubic phase. (a) Total (multiband) Fermi surface of magnetite as derived from the spin-polarized electronic band structure using the WIEN2K code, (b) isolated minority-spin t_{2g} band of interest.

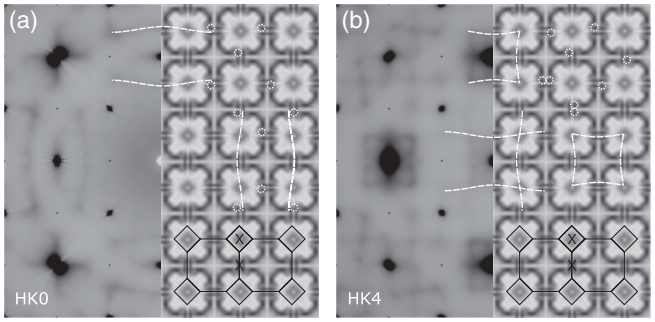

FIG. 6. Nesting signatures in the reciprocal space of magnetite. Selected reciprocal space patterns of magnetite at $T_V + \delta$ [left-hand panels of (a) and (b)] in the (a) HK0 plane and (b) HK4 plane are compared to the Fermi surface nesting construction [right-hand panels of (a) and (b)]. Dark features in the nesting construction correspond to more efficient nesting. Common features are underlined or encircled by dashed lines. The contours of the Brillouin zone are superposed on the right-hand subpanels, X points are indicated. Note that the X point is avoided, in both the experiment and the calculation.

parts of the squares and arcs observed in the diffuse scattering, and indicated by the dashed lines, can be found in the nesting construction. Additionally, the strong arcs inside the squares are fully reproduced. The spots with high intensity close to the X points are indicated by circles. Not all features obtained from calculations can be observed in the diffuse scattering patterns as the nesting construction does not take into account the modulation related to the x-ray structure factor of the spinel structure, which should attenuate or suppress a number of features compared to others. The real Q dependence would take into account the structure factor arising from the average crystallographic positions and polaron-related displacements.

The absence of an efficient nesting vector directing to the X point is reflected in the displacement of the maximum of diffuse scattering away from this point. The origin of this displacement is not clear, but it points towards an incommensurate character of short-range fluctuations and is consistent with the recent inelastic x-ray scattering studies [35].

We emphasize that the agreement between the diffuse scattering data and the calculated Fermi surface nesting, shown in Fig. 6, is remarkable. The matching between the observed data and calculated patterns appears to be very good indeed, and this provides clear evidence that scattering within the minority-spin *d* band accounts for the diffuse scattering, and hence, Fermi surface nesting may, in part, explain the nature of the Verwey transition.

V. SUMMARY

In summary, our diffuse scattering study of magnetite allows us to link the nature of short-range charge ordering above the Verwey temperature with the long-range structure of the low-T phase. The short-range correlations generate a very rich pattern in large areas of reciprocal space with the highest intensities shifted from commensurate wavelengths. The complexes of trimerons are inherited from the low-T structure with minor modifications. Their characteristic correlation length can be on the order of ~1.5 nm just above T_V, and a local symmetry lower than cubic can be assumed.

In this context, the study of external stimuli on the diffuse scattering pattern (i.e., magnetic field) might be interesting, as it could reduce the symmetry of diffuse scattering without major changes in the average cubic structure. The coupling between charge fluctuations and lattice distortions (phonons) leads ultimately to the structural phase transition with a complicated charge distribution. The underlying mechanism for the formation of nontrivial charge ordering can be related to nesting features of the Fermi surface and thus to the Fermi surface shape. We previously demonstrated an example of successful use of Fermi surface reconstruction via 3D reciprocal space mapping associated with the electron-phonon coupling [48], and now we show that this approach can be extended well beyond the "good" metals.

The most straightforward methods of Fermi surface measurements would fail in the case of magnetite—for example, the de Haas–van Alphen and Shubnikov–de Haas effects, as well as positron annihilation, cannot be used due to the required low temperatures at which Fe_3O_4 is insulating. The use of photoemission spectroscopy is far from being obvious due to the highly polar surface terminations that distort the electronic structure within the shallow probing depth, and potentially due to the surface instability under UHV conditions. Thus, providing constraints on the Fermi surface of magnetite from the diffuse scattering appears to be particularly attractive.

ACKNOWLEDGMENTS

A. B. acknowledges Clemens Schulze-Briese for access to beam line X06SA at the SLS and Daniele De Sanctis for access to beam line ID29 at the ESRF. P. P. and A. M. O. acknowledge support by the Polish National Science Center (NCN) under Projects No. 2011/01/M/ST3/00738 and No. 2012/04/A/ST3/00331.

[1] E. J. W. Verwey, *Electronic Conduction of Magnetite (Fe_3O_4) and Its Transition Point at Low Temperatures*, Nature (London) **144**, 327 (1939).

[2] M. Iizumi, T. F. Koetzle, G. Shirane, S. Chikazumi, M. Matsui, and S. Todo, *Structure of Magnetite (Fe_3O_4) below the Verwey Transition Temperature*, Acta Crystallogr. Sect. B **38**, 2121 (1982).

[3] M. Imada, A. Fujimori, and Y. Tokura, *Metal-Insulator Transitions*, Rev. Mod. Phys. **70**, 1039 (1998).

[4] F. Walz, *The Verwey Transition—A Topical Review*, J. Phys. Condens. Matter **14**, R285 (2002).

[5] M. Fähnle, H. Kronmüller, and F. Walz, *Time Scales of Electronic Processes: An Attempt to Resolve a Recently Accentuated Controversy*, Physica (Amsterdam) **369B**, 177 (2005).

[6] J. P. Wright, J. P. Attfield, and P. G. Radaelli, *Long-Range Charge Ordering in Magnetite below the Verwey Transition*, Phys. Rev. Lett. **87**, 266401 (2001).

[7] J. P. Wright, J. P. Attfield, and P. G. Radaelli, *Charge-Ordered Structure of Magnetite Fe_3O_4 below the Verwey Transition*, Phys. Rev. B **66**, 214422 (2002).

[8] J. García and G. Subias, *The Verwey Transition—A New Perspective*, J. Phys. Condens. Matter **16**, R145 (2004).

[9] M. S. Senn, J. P. Wright, and J. P. Attfield, *Charge Order and Three-Site Distortions in the Verwey Structure of Magnetite*, Nature (London) **481**, 173 (2012).

[10] I. Leonov, A. N. Yaresko, V. N. Antonov, M. A. Korotin, and V. I. Anisimov, *Charge and Orbital Order in Fe_3O_4*, Phys. Rev. Lett. **93**, 146404 (2004).

[11] H.-T. Jeng, G. Y. Guo, and D. J. Huang, *Charge-Orbital Ordering and Verwey Transition in Magnetite*, Phys. Rev. Lett. **93**, 156403 (2004).

[12] P. Piekarz, K. Parlinski, and A. M. Oleś, *Mechanism of the Verwey Transition in Magnetite*, Phys. Rev. Lett. **97**, 156402 (2006).

[13] P. Piekarz, K. Parlinski, and A. M. Oleś, *Origin of the Verwey Transition in Magnetite: Group Theory, Electronic Structure, and Lattice Dynamics Study*, Phys. Rev. B **76**, 165124 (2007).

[14] H. P. Pinto and S. D. Elliott, *Mechanism of the Verwey Transition in Magnetite: Jahn-Teller Distortion and Charge-Ordering Patterns*, J. Phys. Condens. Matter **18**, 10427 (2006).

[15] E. Nazarenko, J. E. Lorenzo, Y. Joly, J. L. Hodeau, D. Mannix, and C. Marin, *Resonant X-Ray Diffraction Studies on the Charge Ordering in Magnetite*, Phys. Rev. Lett. **97**, 056403 (2006).

[16] J. E. Lorenzo, C. Mazzoli, N. Jaouen, C. Detlefs, D. Mannix, S. Grenier, Y. Joly, and C. Marin, *Charge and Orbital Correlations at and above the Verwey Phase Transition in Magnetite*, Phys. Rev. Lett. **101**, 226401 (2008).

[17] J. Schlappa, C. Schüßler-Langeheine, C. F. Chang, H. Ott, A. Tanaka, Z. Hu, M. W. Haverkort, E. Schierle, E. Weschke, G. Kaindl, and L. H. Tjeng, *Direct Observation of t_{2g} Orbital Ordering in Magnetite*, Phys. Rev. Lett. **100**, 026406 (2008).

[18] J. Blasco, J. García, and G. Subías, *Structural Transformation in Magnetite below the Verwey Transition*, Phys. Rev. B **83**, 104105 (2011).

[19] A. Tanaka, C. F. Chang, M. Buchholz, C. Trabant, E. Schierle, J. Schlappa, D. Schmitz, H. Ott, P. Metcalf, L. H. Tjeng, and C. Schüßler-Langeheine, *Symmetry of Orbital Order in Fe_3O_4 Studied by $FeL_{2,3}$ Resonant X-Ray Diffraction*, Phys. Rev. Lett. **108**, 227203 (2012).

[20] G. Subías, J. García, J. Blasco, J. Herrero-Martin, M. C. Sánchez, J. Orna, and L. Morellón, *Structural Distortion, Charge Modulation and Local Anisotropies in Magnetite below the Verwey Transition Using Resonant X-Ray Scattering*, J. Synchrotron Radiat. **19**, 159 (2012).

[21] M. S. Senn, I. Loa, J. P. Wright, and J. P. Attfield, *Electronic Orders in the Verwey Structure of Magnetite*, Phys. Rev. B **85**, 125119 (2012).

[22] D. Ihle and B. Lorenz, *Small-Polaron Conduction and Short-Range Order in Fe_3O_4*, J. Phys. C **19**, 5239 (1986).

[23] S. K. Park, T. Ishikawa, and Y. Tokura, *Charge-Gap Formation upon the Verwey Transition in Fe_3O_4*, Phys. Rev. B **58**, 3717 (1998).

[24] D. Schrupp, M. Sing, M. Tsunekawa, H. Fujiwara, S. Kasai, A. Sekiyama, S. Suga, T. Muro, V. A. M. Brabers, and R. Claessen, *High-Energy Photoemission on Fe_3O_4: Small Polaron Physics and the Verwey Transition*, Europhys. Lett. **70**, 789 (2005).

[25] G. Subías, J. García, and J. Blasco, *EXAFS Spectroscopic Analysis of the Verwey Transition in Fe_3O_4*, Phys. Rev. B **71**, 155103 (2005).

[26] T. J. Moran and B. Lüthi, *Elastic and Magnetoelastic Effects in Magnetite*, Phys. Rev. **187**, 710 (1969).

[27] H. Schwenk, S. Bareiter, C. Hinkel, B. Lüthi, Z. Kąkol, A. Kozłowski, and J. M. Honig, *Charge Ordering and Elastic Constants in $Fe_{3-x}Zn_xO_4$*, Eur. Phys. J. B **13**, 491 (2000).

[28] M. M. Seikh, C. Narayana, P. A. Metcalf, J. M. Honig, and A. K. Sood, *Brillouin Scattering Studies in Fe_3O_4 across the Verwey Transition*, Phys. Rev. B **71**, 174106 (2005).

[29] Y. Fujii, G. Shirane, and Y. Yamada, *Study of the 123 K Phase Transition of Magnetite by Critical Neutron Scattering*, Phys. Rev. B **11**, 2036 (1975).

[30] K. Chiba, K. Suzuki, and S. Chikazumi, *Diffuse Electron Scattering from Magnetite above the Verwey Transition Temperature*, J. Phys. Soc. Jpn. **39**, 839 (1975).

[31] S. M. Shapiro, M. Iizumi, and G. Shirane, *Neutron Scattering Study of the Diffuse Critical Scattering Associated with the Verwey Transition in Magnetite (Fe_3O_4)*, Phys. Rev. B **14**, 200 (1976).

[32] Y. Yamada, N. Wakabayashi, and R. M. Nicklow, *Neutron Diffuse Scattering in Magnetite due to Molecular Polarons*, Phys. Rev. B **21**, 4642 (1980).

[33] R. Aragón, P. M. Gehring, and S. M. Shapiro, *Stoichiometry, Percolation, and Verwey Ordering in Magnetite*, Phys. Rev. Lett. **70**, 1635 (1993).

[34] K. Siratori, Y. Ishii, Y. Morii, S. Funahashi, S. Todo, and A. Yanase, *Neutron Diffuse Scattering Study of the High-Temperature Phase of Fe_3O_4—I. Determination of Atomic Displacements at the X Point in the Brillouin Zone*, J. Phys. Soc. Jpn. **67**, 2818 (1998).

[35] M. Hoesch, P. Piekarz, A. Bosak, M. Le Tacon, M. Krisch, A. Kozłowski, A. M. Oleś, and K. Parlinski, *Anharmonicity due to Electron-Phonon Coupling in Magnetite*, Phys. Rev. Lett. **110**, 207204 (2013).

[36] R. Aragón and R. H. McCallister, *Phase and Point Defect Equilibria in the Titanomagnetite Solid Solution*, Phys. Chem. Miner. **8**, 112 (1982).

[37] R. Aragón, H. R. Harrison, R. H. McCallister, and C. J. Sandberg, *Skull Melter Single Crystal Growth of Magnetite (Fe_3O_4)-Ulvospinel (Fe_2TiO_4) Solid Solution Members*, J. Crystal Growth **61**, 221 (1983).

[38] F. Walz, V. A. M. Brabers, J. H. V. J. Brabers, and H. Kronmüller, *Vacancy-Interstitial Annihilation in Titanomagnetite by Thermal Annealing*, Phys. Status Solidi A **204**, 3514 (2007).

[39] See Supplemental Material at http://link.aps.org/supplemental/10.1103/PhysRevX.4.011040 for more technical details.

[40] V. Chlan, K. Kouril, H. Štepánková, R. Reznicek, J. Stepanek, W. Tabis, G. Krol, Z. Tarnawski, Z. Kakol, and A. Kozlowski, *Magnetically Induced Structural Reorientation in Magnetite Studied by Nuclear Magnetic Resonance*, J. Appl. Phys. **108**, 083914 (2010).

[41] P. Novák, H. Štepánková, J. Englich, J. Kohout, and V. A. M. Brabers, *NMR in Magnetite below and around the Verwey Transition*, Phys. Rev. B **61**, 1256 (2000).

[42] C. Broennimann, E. F. Eikenberry, B. Henrich, R. Horisberger, G. Huelsen, E. Pohl, B. Schmitt, C. Schulze-Briese, M. Suzuki, T. Tomizaki, H. Toyokawa, and A. Wagner, *The PILATUS 1 M detector*, J. Synchrotron Radiat. **13**, 120 (2006).

[43] CrysAlis software, version 1.171.32.40 (Oxford-Diffraction Ltd., Oxford, England).

[44] P. Blaha, K. Schwarz, G. K. H. Madsen, D. Kvasnicka, and J. Luitz, Wien2k: *An Augmented Plane Wave + Local Orbitals Program for Calculating Crystal Properties* (Technische Universität Wien, Austria, 2001).

[45] M. A. Krivoglaz, *Diffuse Scattering of X Rays and Neutrons by Fluctuations* (Springer, Berlin, 1996).

[46] H. Reichert, S. C. Moss, and K. S. Liang, *Anomalous Temperature Dependence of the X-Ray Diffuse Scattering Intensity of Cu_3Au*, Phys. Rev. Lett. **77**, 4382 (1996).

[47] N. W. Ashcroft and N. D. Mermin, *Solid-State Physics* (Holt-Saunders International Eds., Philadelphia, 1976).

[48] A. Bosak, M. Hoesch, M. Krisch, D. Chernyshov, P. Pattison, C. Schulze-Briese, B. Winkler, V. Milman, K. Refson, D. Antonangeli, and D. Farber, *3D Imaging of the Fermi Surface by Thermal Diffuse Scattering*, Phys. Rev. Lett. **103**, 076403 (2009).